Wiley
International Journal of Energy Research
Volume 2025, Article ID 9740805, 16 pages
https://doi.org/10.1155/er/9740805

Research Article

Amorphous Vanadium Oxide Nanoparticle-Impregnated Three-Dimensional Reduced Graphene Oxide and Nitrogen-Doped Carbon Nanotubes Composite Microspheres as Functional Interlayers for Lithium–Sulfur Batteries

Kun Woo Baek,[1] **Sang-Hyun Kim**,[2] **Jung Sang Cho**,[1,3,4] **and Gi Dae Park**[2,4,5]

[1]*Department of Engineering Chemistry, Chungbuk National University, Cheongju 361-763, Chungbuk, Republic of Korea*
[2]*Department of Urban, Energy, and Environmental Engineering, Chungbuk National University, Cheongju 361-763, Chungbuk, Republic of Korea*
[3]*Biomedical Research Institute, Chungbuk National University Hospital, Cheongju 28644, Chungbuk, Republic of Korea*
[4]*Advanced Energy Research Institute, Chungbuk National University, Cheongju 28644, Chungbuk, Republic of Korea*
[5]*Department of Advanced Materials Engineering, Chungbuk National University, Cheongju 361-763, Chungbuk, Republic of Korea*

Correspondence should be addressed to Jung Sang Cho; jscho@cbnu.ac.kr and Gi Dae Park; gdpark@chungbuk.ac.kr

Received 22 May 2024; Accepted 31 January 2025

Academic Editor: Yong Pan

Herein, amorphous vanadium oxide (a-VO_x) nanoparticle-impregnated three-dimensional (3D) microspheres comprising highly conductive and porous reduced graphene oxide (rGO) and nitrogen-doped carbon nanotubes (N-CNTs) framework (a-VO_x@rGO-N-CNTs) were designed as functional interlayers for lithium–sulfur batteries (LSBs). N-CNTs were successfully formed on the rGO sheet surfaces, uniformly distributed between rGO and mesopores, via the catalytic effect of metallic Co–Fe. The rGO and N-CNTs framework not only provided an additional pathway for electron transport but also improved structural durability of the electrode materials. Moreover, polar a-VO_x nanoparticles involved within the conduction pathway offered numerous chemisorption sites for anchoring polysulfides, thereby improving the utilization of active materials. The cell employing a-VO_x@rGO-N-CNTs-coated separator as a functional interlayer exhibited excellent rate capabilities (473 mA h g^{-1} at 1.5 C) and cycling performance (800 cycles at 1.0 C and an average decay rate of 0.09% per cycle) at high C-rate. This outstanding performance was mainly ascribed to the synergistic effects of rGO, N-CNTs framework, and polar a-VO_x nanoparticles. The design strategy proposed in this study offers insights into the development of porous and conductive nanostructures for extensive energy storage applications including LSBs.

Keywords: functional interlayer; lithium–sulfur batteries; nitrogen-doped carbon nanotubes; reduced graphene oxide; spray pyrolysis

1. Introduction

Currently, Li-ion batteries (LIBs) dominate the field of energy storage and are widely used in an extensive range of portable electronic devices and electric vehicles [1–6]. With the increasing demand for power grids or energy storage systems, LIBs are reaching their theoretical limits in terms of gravimetric and volumetric energy densities, prompting the exploration of alternative materials with higher energy/volume densities [5, 7, 8]. In this regard, lithium–sulfur batteries (LSBs) have been considered as next-generation energy storage devices capable of replacing LIBs owing to their exceptionally high energy densities (2600 Wh kg^{-1}), high theoretical capacities (1675 mA h g^{-1}), suitable average operating voltages (~2.1 V vs. Li/Li^+), and the abundance of elemental S [5, 9–12]. Nevertheless, the applications of LSBs are hindered by some challenges including low electrical conductivities of elemental S and discharge products, reducing active material utilization [13–16]. Migration of lithium–polysulfides (LiPSs) toward the Li anode leads to material loss due to the "shuttle effect," and additionally, volume expansion during the conversion of LiPSs induces electrode polarization [17–20].

Related ongoing efforts involve the employment of functional interlayers, which are a promising approach to address the critical shortcomings of LSBs mentioned earlier. Functional interlayers operate through electrocatalytic conversion to adsorb LiPSs migrating toward the Li anode, thereby effectively suppressing the shuttle effect and enhancing the active material utilization [21–25]. Carbonaceous materials, such as carbon nanotubes (CNTs) [26], carbon nanowires [27], graphene oxide (GO) [28], and porous activated carbon [29], have been employed as interlayers because of their excellent electrical conductivities, mechanical strengths, and the presence of macro- and meso-pores. However, despite providing physical adsorption sites for polar LiPSs, nonpolar carbonaceous materials face limitations in effectively suppressing the shuttle effect due to their inherently weak interactions with LiPSs [30–32]. To overcome the limitations of carbonaceous materials, polar materials, including alloys [33], metal oxides [34], nitrides [5], sulfides [35], and phosphides [36], and heteroelement (—N, —O, —P, and —S) doping [37] have been utilized to chemically anchor LiPSs [38, 39]. Therefore, combining carbonaceous materials with metal compounds is necessary to achieve efficient adsorption and conversion of LiPSs.

Graphene, a two-dimensional (2D) material, has gained attention as a carbonaceous material owing to its outstanding physical and electrical properties, effectively mitigating charge-transfer resistance (R_{ct}) during charge–discharge [28, 40–42]. Nevertheless, the chemical reduction of GO for energy-related applications leads to the persistent issue of irreversible aggregation of graphene layers due to van der Waals interactions between them [43–46]. Various studies have been conducted to address this irreversible aggregation [44, 47, 48]. Recently, the preparation of graphene with a paper-ball-like morphology and introduction of CNTs as spacers between graphene layers have attracted attention for strengthening the resistances of graphene layers against aggregation [49]. Among the various synthesis methods, in particular, chemical vapor deposition (CVD) method has mainly been adopted [50]. This process employs transition metal nanocrystals present on the surface of graphene as catalysts to facilitate the vertical growth of CNTs between graphene layers. The resulting graphene composites feature CNTs that interconnect graphene sheets, effectively preventing restacking. These composites exhibit outstanding mechanical and electrical properties and have been reported to show enhanced electrochemical performance when utilized as anode materials [51, 52].

Accordingly, in this study, a new strategy for the fabrication of metal oxide-3D (three-dimensional) reduced GO (rGO) and N-doped CNTs composite microspheres (metal oxide@rGO-N-CNTs) is successfully reported, involving spray pyrolysis, CVD, and a simple drop-and-dry process. Amorphous vanadium oxide (a-VO_x)@rGO-N-CNTs are prepared as the first target material. The redox potential of VO_x is slightly higher than those of LiPSs (~2.4 V), contrary to the cases of other metal oxides such as TiO_2, Co_3O_4, and Cu_2O. This is attributed to the high reactivity of VO_x toward LiPSs and enables efficient anchoring of high-order Li_2S_x ($x \geq 4$). Furthermore, the amorphous phase, whose open framework affords multiple penetration pathways, enhances the ion mobilities and charge storage capabilities of rGO-N-CNTs, thereby improving the conductivities of electrode materials. Moreover, a-VO_x@rGO-N-CNTs have been applied as functional interlayers in LSBs, exhibiting stable cycling performances and excellent rate capabilities.

2. Materials and Methods

Crumpled rGO microspheres were prepared by spray pyrolysis. During spray pyrolysis, droplets were generated using a 1.7 MHz ultrasonic spray generator consisting of six vibrators. Spray solution was fabricated by dissolving 0.02 M $Co(NO_3)_2{\cdot}6H_2O$ (98.0%, Junsei) and $Fe(NO_3)_3{\cdot}9H_2O$ (98.5%, Samchun chemical) in a 1:1 ratio, 1.0 mg mL^{-1} GO, and 1.0 g mL^{-1} of 100 nm polystyrene (PS) nanobeads in 500 mL distilled water. GO was synthesized from graphite flakes using a modified Hummer's method [53], and PS nanobeads were prepared using emulsion polymerization, as described in our previous study [54]. The droplets were transferred to a quartz reactor, with a length of 1200 mm and diameter of 50 mm, and the temperature of the reactor was maintained at 400°C using air as the carrier gas at a flow rate of 20 L min^{-1}. To form rGO-N-CNTs, the sprayed precursor was subjected to CVD with dicyandiamide (DCDA) in a tube furnace. The process involved heating the sprayed precursor at 300°C for 3 h, followed by subsequent heating at 750°C for 2 h at a rate of 5°C min^{-1} under a 10% H_2/Ar atmosphere. Based on 1.0 g rGO-N-CNTs powder, 1.5 g vanadyl acetylacetonate ($C_{10}H_{14}O_5V$, Samchun Chemical) was dissolved in high-purity ethyl alcohol. The resulting solution was introduced into the rGO-N-CNTs powder. Oxidation at 250°C for 3 h under an air atmosphere transformed $C_{10}H_{14}O_5V$@rGO-N-CNTs into a-VO_x@rGO-N-CNTs. Detailed information about the characterizations and electrochemical measurements of the prepared samples is provided in the Supporting Information.

3. Results and Discussion

Procedure for the synthesis of a-VO_x@rGO-N-CNTs is depicted in Scheme 1. Spray pyrolysis was specifically used to produce microsphere composites of metal salts and polymers in a uniformly dispersed state within the spray solution. Droplets generated by the ultrasonic nebulizer contained evenly dispersed GO nanosheets, cobalt and iron ions, and PS nanobeads. As the droplets passed through the tubular reactor maintained at 400°C using the carrier gas, GO nanosheets converted into crumpled rGO microspheres, whereas Co–Fe oxide nanocrystals were homogeneously dispersed on the rGO surface, and the PS nanobeads were surrounded by rGO nanosheets. Thereafter, the sprayed precursor was post-treated with DCDA under an inert atmosphere to synthesize rGO-N-CNTs. In the initial step of this process, metallic Co–Fe alloys formed via the reduction of Co–Fe oxide nanocrystals, while the PS nanobeads

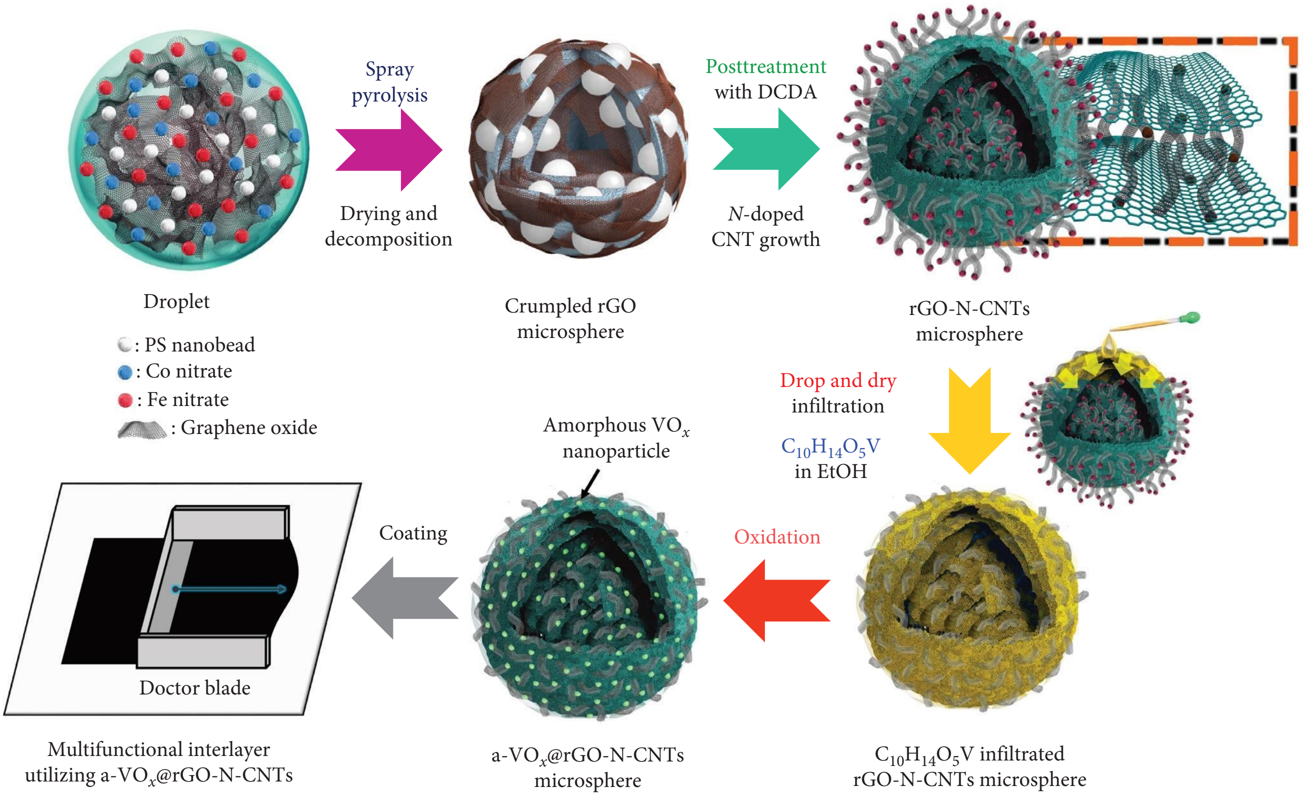

Scheme 1: Schematic representation of formation mechanism of a-VO_x@rGO-N-CNTs microspheres.

decomposed, resulting in uniform pores with a mean size of 100 nm inside the microspheres. In the subsequent step, metallic Co–Fe facilitated N-CNT growth from the carbon nitride gas generated by the decomposition of DCDA through its catalytic effect. Moreover, N-CNTs grew inside the microspheres, utilizing the pores derived from the decomposition of PS nanobeads. The resulting rGO-N-CNTs microspheres with high pore volumes served as templates for the infiltration of metal salt solution. Vanadyl acetylacetonate, used as the vanadium source, was dissolved in high-purity ethyl alcohol followed by infiltration into rGO-N-CNTs using the drop-and-dry process. Vanadium salt solution impregnated in the microspheres transformed into a-VO_x nanoparticles via oxidation at a low temperature of 250°C. Finally, the obtained a-VO_x@rGO-N-CNTs were coated on a commercial Celgard separator, and the resulting separator was applied as a functional interlayer for an LSBs.

Morphological and crystal structure characteristics of the sprayed precursor are shown in Figure S1. The sprayed precursor demonstrates a crumpled ball morphology, consisting of 2D structured graphene sheets and spherical shape with a smooth surface (Figure S1a,b), which is attributed to the undecomposed PS nanobeads. X-ray diffraction (XRD) pattern of the sprayed precursor (Figure S1c) is broad with no discernible peaks, indicating that the Co–Fe oxide nanocrystals exist in extremely small sizes, and PS nanobeads are in less degraded states. Morphological characteristics of rGO-N-CNTs synthesized via posttreatment of the sprayed precursor with DCDA are depicted in Figure 1. Low-magnification scanning electron microscopy (SEM) image shown in Figure 1a confirms the uniform growth of CNTs on the crumpled rGO microsphere surfaces via the catalytic effect of metallic Co–Fe. Transmission electron microscopy (TEM) images (Figure 1b,c) reveal even growths of CNTs inside the rGO microspheres owing to the catalytic effect of metallic Co–Fe distributed throughout the microspheres. Moreover, the porous structures of rGO-N-CNTs are verified to be generated by the decomposition of PS nanobeads, and these microspheres exhibit hierarchical structures in which graphene layers are interconnected by N-CNTs. High-resolution (HR)-TEM image (Figure 1d) demonstrates clear lattice fringes separated by the interplanar spacings of 0.20 and 0.21 nm corresponding to the (110) and (330) crystal planes of Co_3Fe_7 and $Co_{0.72}Fe_{0.28}$ phase. Selected area electron diffraction (SAED) pattern (Figure 1e) indicates the existences of Co_3Fe_7 and $Co_{0.72}Fe_{0.28}$ phase. Elemental mapping image (Figure 1f) reveals homogeneous distribution of Co–Fe in the carbon matrices of rGO and CNTs. Additionally, the N signal is associated with N-CNTs grown by the decomposition of DCDA. N-CNTs improve the electrical conductivities of the electrode materials and facilitate the anchoring of LiPSs.

Morphological characteristics of a-VO_x@rGO-N-CNTs, which were prepared from rGO-N-CNTs via the drop-and-dry process using a vanadium salt solution, are shown in Figure 2. Low-magnification SEM images (Figure 2a) demonstrate that the surfaces of a-VO_x@rGO-N-CNTs are smoother compared to those of rGO-N-CNTs (low-magnification SEM images shown in Figure 1a), which implies uniform

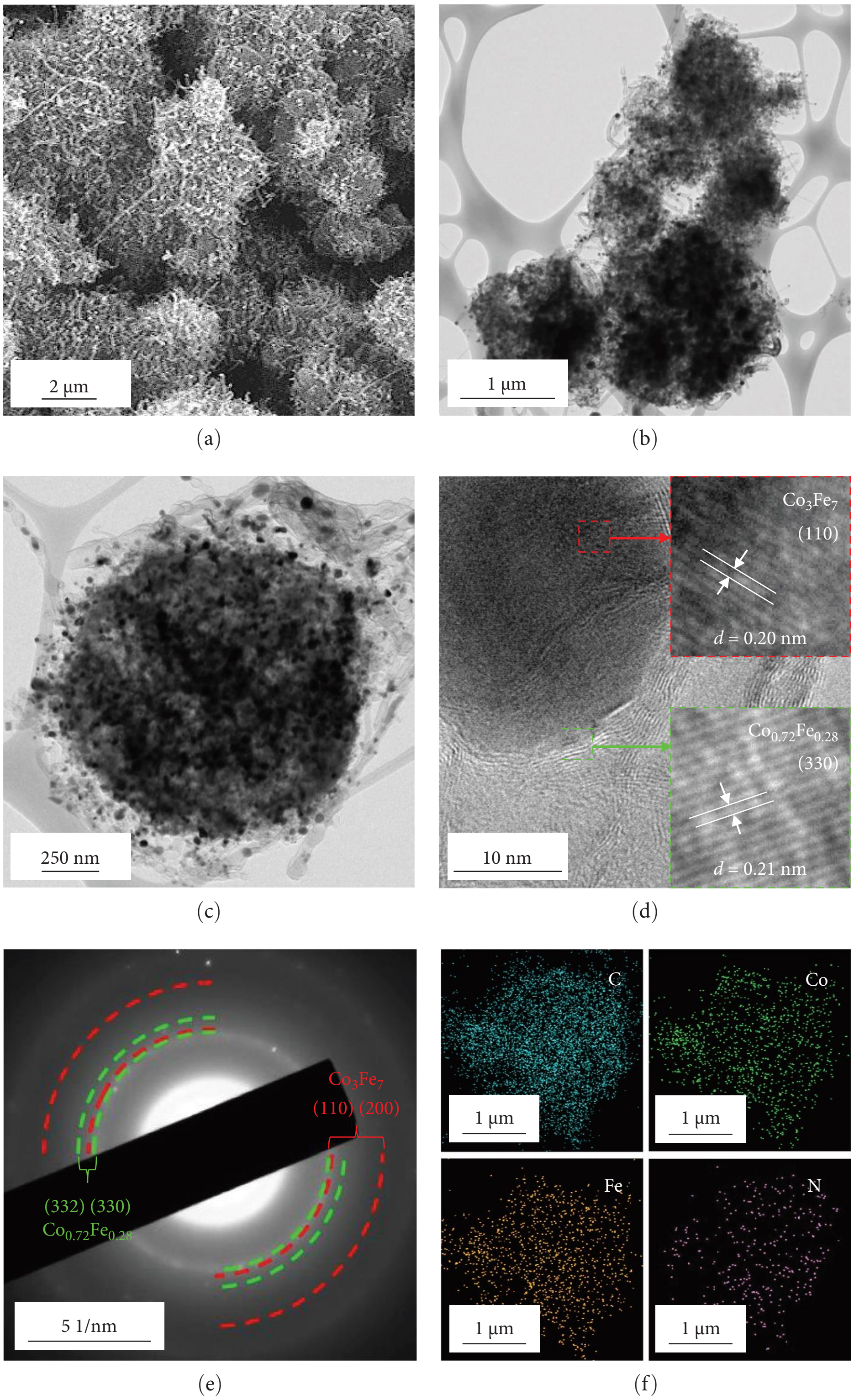

Figure 1: Morphologies, SAED, and elemental mapping images of rGO-N-CNTs microspheres obtained after heat-treatment of sprayed precursor assisted by DCDA: (a) FE-SEM image, (b, c) TEM images, (d) HR-TEM image, (e) SAED pattern, and (f) elemental mapping images. SAED, selected area electron diffraction; TEM, transmission electron microscopy.

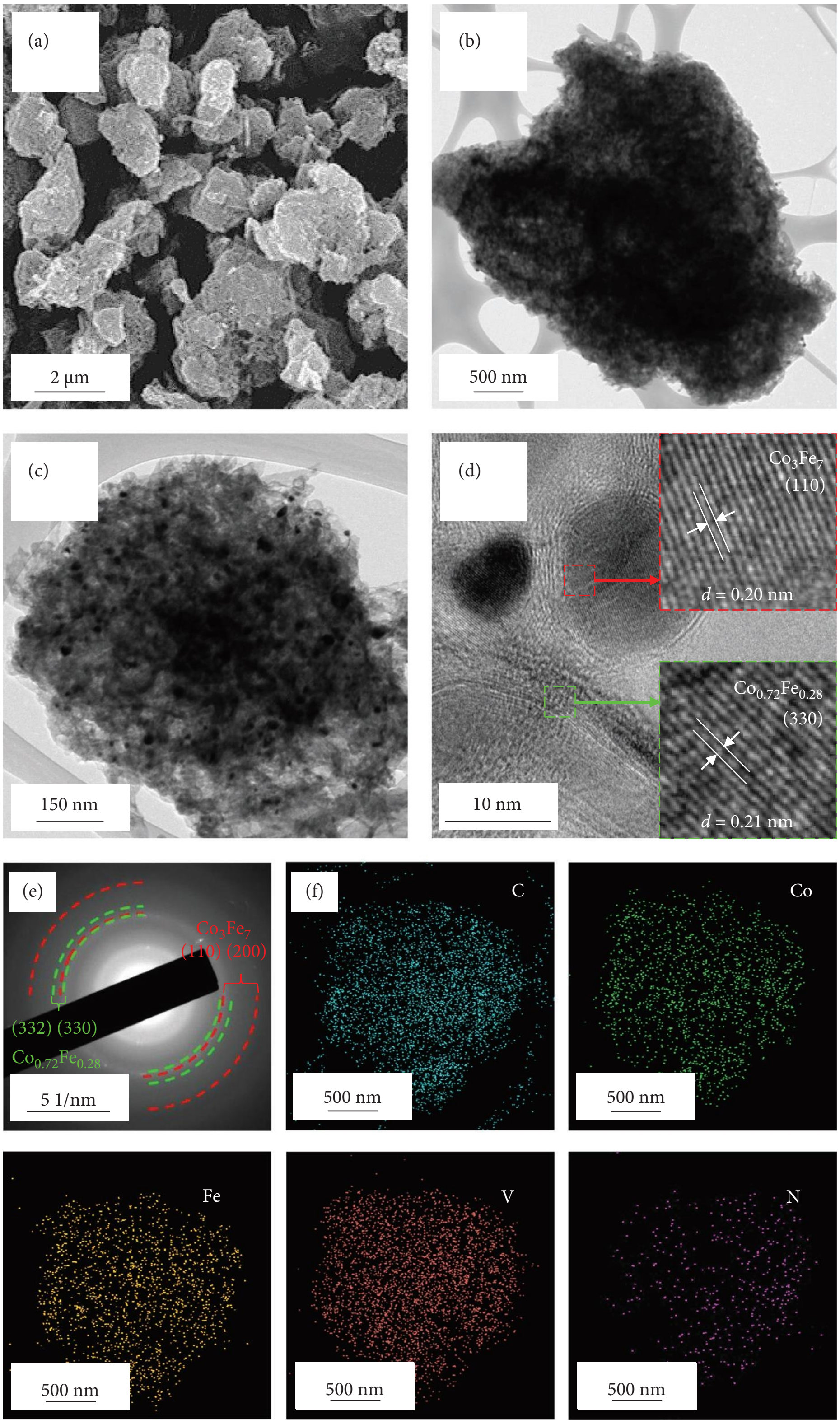

Figure 2: Morphologies, SAED, and elemental mapping images of a-VO$_x$@rGO-N-CNTs microspheres obtained after drop-and-dry process of vanadium solution and oxidation at 250°C: (a) FE-SEM image, (b, c) TEM images, (d) HR-TEM image, (e) SAED pattern, and (f) elemental mapping images. SAED, selected area electron diffraction; TEM, transmission electron microscopy.

impregnation of a-VO_x nanocrystals throughout the microsphere surfaces. TEM images (Figure 2b,c) indicate that rGO-N-CNTs are sufficiently filled with a-VO_x nanoparticles. Moreover, the characteristics of rGO-N-CNTs are appropriately retained even after oxidation, and these microspheres serve as stable templates for the infiltration of vanadium salt solution. HR-TEM image (Figure 2d) reveals lattice fringes separated by 0.20 and 0.21 nm corresponding to the (110) and (330) crystal planes of Co_3Fe_7 and $Co_{0.72}Fe_{0.28}$ phase. Absence of the lattice fringe related to VO_x is ascribed to the amorphous phase resulting from oxidation conducted at a low temperature of 250°C. SAED pattern (Figure 2e) demonstrates the presence of Co_3Fe_7 and $Co_{0.72}Fe_{0.28}$ phase. Corresponding elemental mapping images (Figure 2f) confirm the existence of Co–Fe in the carbon matrix along with N-CNTs. Furthermore, the V signal clearly implies that the a-VO_x nanoparticles are homogeneously dispersed in the C matrix.

XRD patterns of rGO-N-CNTs and a-VO_x@rGO-N-CNTs are depicted in Figure S2. In the XRD pattern of a-VO_x@rGO-N-CNTs, the absence of peaks related to VO_x comfirm the presence of amorphous VO_x nanoparticles. Additionally, the XRD patterns of both samples exhibit diffraction peaks associated with $Co_{0.72}Fe_{0.28}$ and Co_3Fe_7 phase, which act as catalysts for CNT growth. Chemical states of the several elements in a-VO_x@rGO-N-CNTs were evaluated by X-ray photoelectron spectroscopy (XPS) (Figure 3). HR V 2p spectrum of a-VO_x@rGO-N-CNTs (Figure 3a) demonstrates V $2p_{3/2}$ and V $2p_{1/2}$ orbital peaks related to V^{4+}/V^{5+} oxidation states at the binding energies of 516.3/517.0 and 523.5/524.3 eV, respectively [55, 56]. The V^{5+} oxidation state is attributed to the oxidation of vanadium components near the surface in contact with air [56, 57].

In the O 1s spectrum (Figure 3b), the three distinct peaks at 529.7, 531.1, and 532.9 eV corresponding to V—O, C═O, C—O, and O—H bonds are clearly observed [58]. Co 2p spectrum (Figure 3c) was deconvoluted into Co $2p_{3/2}$ and Co $2p_{1/2}$ orbital peaks at the binding energies of 780.6 eV and 796.3 eV, respectively. The Co $2p_{3/2}$ (778.6 eV) and Co $2p_{1/2}$ (794.9 eV) peaks are located at binding energies that are in accordance with those of the related peaks of metallic cobalt [59]. Additional Co $2p_{3/2}$ and Co $2p_{1/2}$ peaks are noticed at 780.4/796.2 and 782.2/797.4 eV, respectively, corresponding to Co^{3+} and Co^{2+}, along with four satellite peaks [60–62]. Fe 2p spectrum (Figure 3d) exhibits several doublet peaks at 707.9/722.4, 710.5/724.0, and 712.4/726.4 eV, attributed to metallic Fe, Fe^{2+}, and Fe^{3+}, respectively [59, 63]. Satellite peaks are detected at ~717.1 and 731.3 eV. Deconvoluted N 1s spectrum (Figure 3e) demonstrates three peaks at 398.2, 399.8, and 403.1 eV corresponding to pyridinic N, pyrrolic N, and graphitic N, verifying the existence of N-doped carbon framework [64]. C 1s spectrum (Figure 3f) was deconvoluted into four peaks at 284.3 eV, 285.1 eV, 285.8 eV, and 286.8 eV related to C═C, C—N, C—O, and C═O, respectively [65, 66]. Presence of the peak of C—N bond at 285.1 eV implies the existence of N-CNTs, which improve the electrical conductivities and chemical activities of the electrode materials [22].

Raman spectra of a-VO_x@rGO-N-CNTs and rGO-N-CNTs (Figure 4a) commonly exhibit D-bands near 1354 cm^{-1} and G-bands near 1595 cm^{-1}, respectively. D- and G-bands are characteristic bands of carbonaceous materials, for example, disordered and graphitic carbon materials. The intensity ratios of D- to G-bands (I_D/I_G) for a-VO_x@rGO-N-CNTs and rGO-N-CNTs are 1.02 and 1.07, respectively. Proximities of the I_D/I_G values for the two samples to 1.0 are attributed to the influences of the defects induced by N-CNT growth. Thermogravimetric (TG) curves of a-VO_x@rGO-N-CNTs and rGO-N-CNTs are shown in Figure 4b. To determine the contents of carbon and a-VO_x in a-VO_x@rGO-N-CNTs, XRD pattern of the sample obtained after the oxidation of rGO-N-CNTs at 800°C was analyzed (Figure S3). Considering the oxidized product $CoFe_2O_4$-Co_3O_4, the carbon content of rGO-N-CNTs is calculated as 66.4 wt%. Finally, taking the amount of impregnated vanadyl acetylacetonate into account, the contents of a-VO_x and carbon in a-VO_x@rGO-N-CNTs are evaluated as 31.9 and 45.2 wt%, respectively. Specific surface areas and pore structures of a-VO_x@rGO-N-CNTs and rGO-N-CNTs were evaluated using Brunauer–Emmett–Teller (BET) and Barrett–Joyner–Halenda (BJH) methods. N_2 adsorption–desorption isotherms (Figure S4) demonstrate a combination of type IV and H3 hysteresis loops, indicating the formation of a hierarchical mesoporous structure. BET surface areas of a-VO_x@rGO-N-CNTs and rGO-N-CNTs are 19.2 and 253.4 $m^2\ g^{-1}$, respectively, and the corresponding pore volumes are 0.15 and 0.56 $cm^3\ g^{-1}$. Different tendencies of the specific surface areas and pore volumes of the two samples reveal that the vanadium salt solution is sufficiently absorbed by the interior pores of rGO-N-CNTs, and subsequently, a-VO_x nanoparticles are produced after the oxidation of resulting rGO-N-CNTs.

The physical properties and microstructure analysis of the synthesized a-VO_x@rGO-N-CNTs-coated separator are presented in Figure S5. A digital image of the separator before being punched into a circular disk (Figure S5a) demonstrates a uniform coating without visible cracks. Additionally, Figure S5b shows the mechanical integrity and flexibility of the separator, showing its ability to withstand folding and bending stresses. The cross-sectional FE-SEM image of the pristine Celgard separator (Figure S5c) reveals a thickness of ~26.8 μm. Furthermore, the image of the separator coated with a-VO_x@rGO-N-CNTs (Figure S5d) clearly shows that the coating is evenly applied over the Celgard separator, with a thickness of about 14.3 μm.

Electrochemical behaviors of Li-S cells featuring a-VO_x@rGO-N-CNTs and rGO-N-CNTs-coated separators as functional interlayers are depicted in Figure 5. The initial CV curve acquired at a scan rate of 0.05 mV s^{-1} (Figure 5a) exhibits typical redox reaction characteristics involving elemental S only. For instance, in the CV curves of the cells comprising a-VO_x@rGO-N-CNTs- and rGO-N-CNTs-coated separators, two distinct cathodic peaks are observed at 2.28/2.00 and 2.26/2.00 V, respectively. These peaks correspond to the successive reduction of elemental S to soluble high- and middle-order polysulfides (Li_2S_x; $4 \leq x \leq 8$) as intermediates, followed by conversion of these intermediates to low-order polysulfides (Li_2S_x; $1 \leq x \leq 3$) [34, 36, 67]. Corresponding anodic sweep demonstrates two closely spaced peaks at 2.36/2.41 and

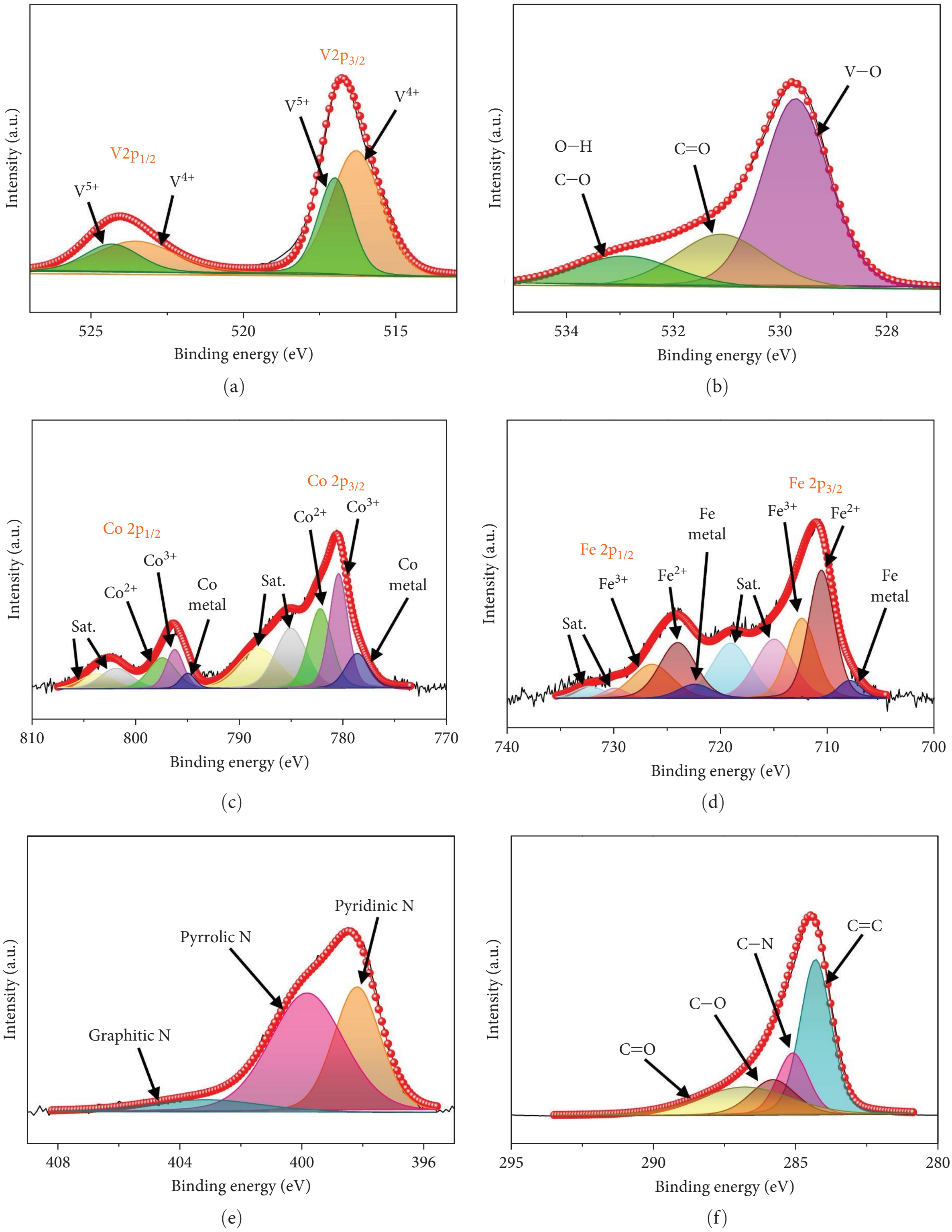

FIGURE 3: XPS spectra of a-VO_x@rGO-N-CNTs microspheres: (a) V 2p, (b) O 1s, (c) Co 2p, (d) Fe 2p, (e) N 1s, and (f) C 1s. XPS, X-ray photoelectron spectroscopy.

2.38/2.44 V for a-VO_x@rGO-N-CNTs- and rGO-N-CNTs-coated separators, respectively. This implies effective transformation of low-order polysulfides to high-order polysulfides and subsequently to elemental S [67–69]. Furthermore, the exactly overlapping CV profiles during the initial five cycles (Figure S6) indicate highly reversible redox processes in the cells. Additionally, the relatively higher current intensities of the cell employing the a-VO_x@rGO-N-CNTs-coated separator as the functional interlayer (Figure 5a) suggests fast redox kinetics. The Li-S cell utilizing the a-VO_x@rGO-N-CNTs-

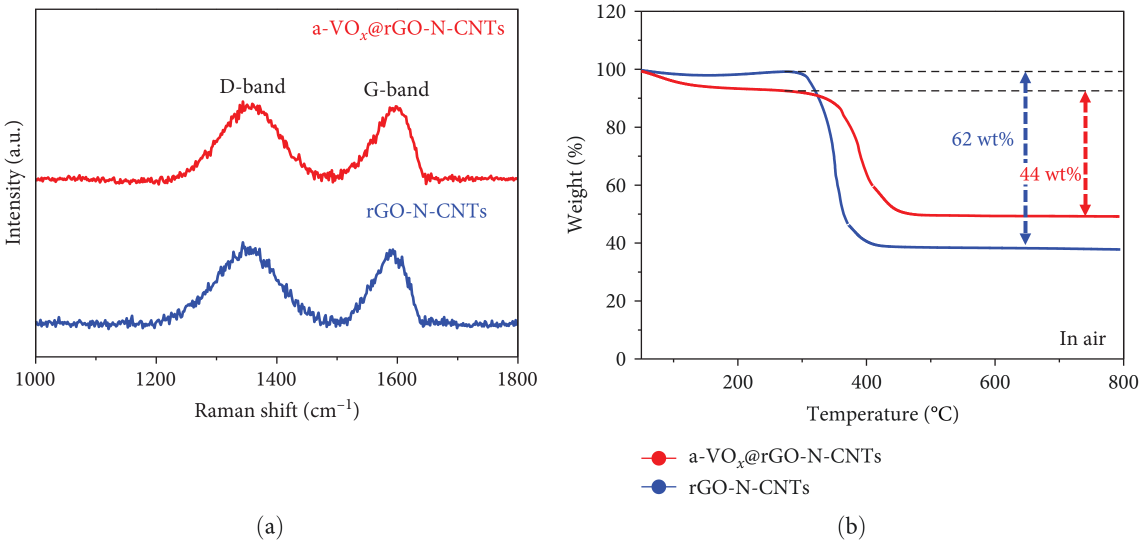

Figure 4: (a) Raman spectrums and (b) TG curves of a-VO$_x$@rGO-N-CNTs and rGO-N-CNTs microspheres. TG, thermogravimetric.

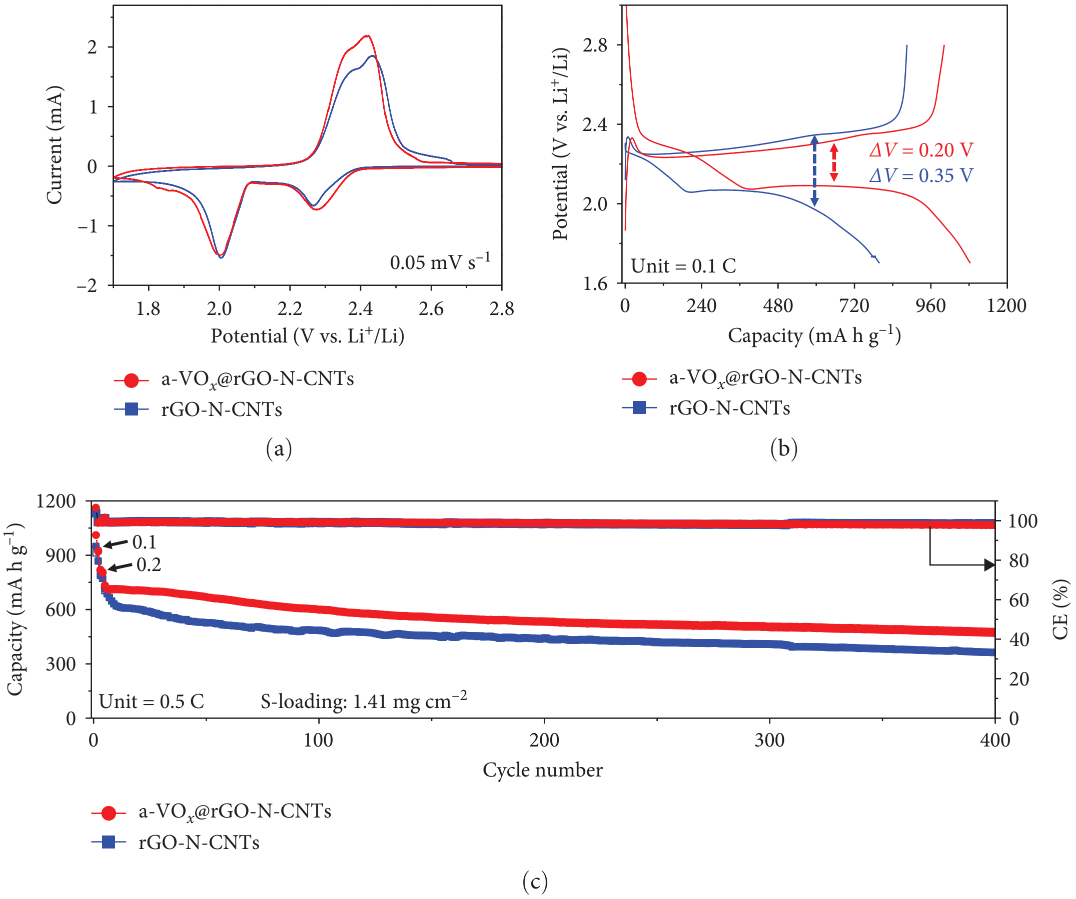

Figure 5: Continued.

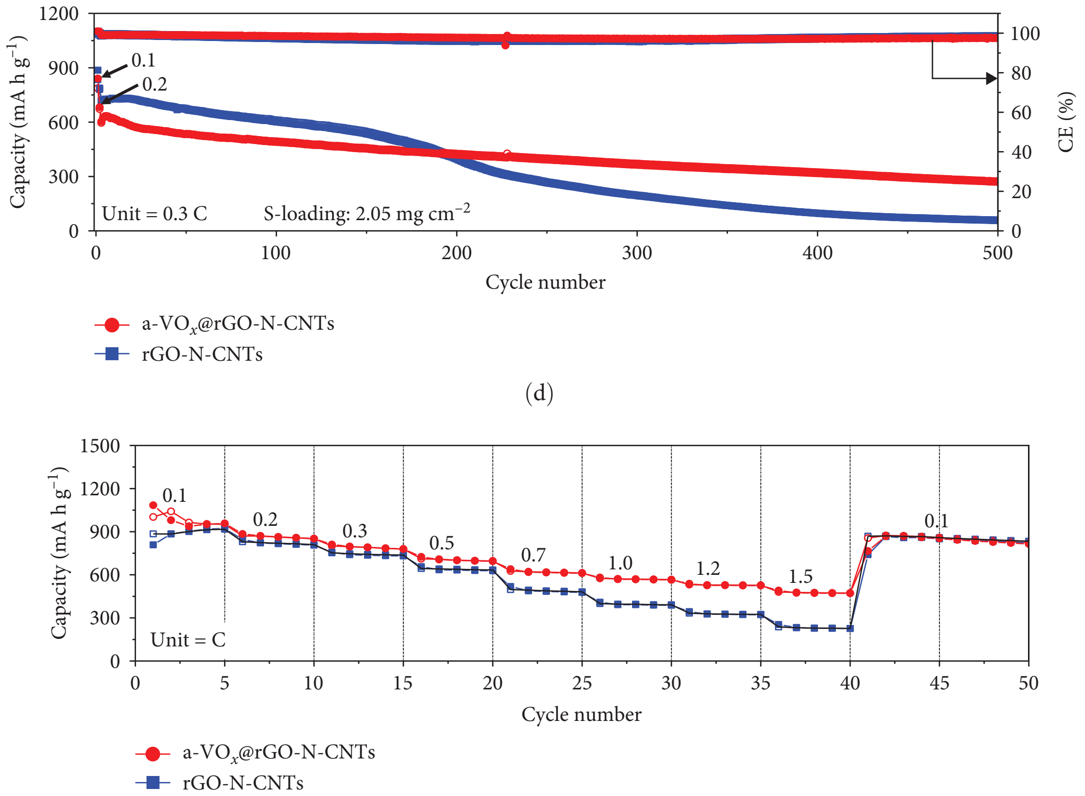

(d)

(e)

FIGURE 5: Electrochemical properties of a-VO$_x$@rGO-N-CNTs and rGO-N-CNTs for Li-S cells: (a) initial CV curves at 0.05 mV S^{-1}, (b) initial charge–discharge potential profiles at 0.1 C, (c) cycle performances of the assembled cells at 0.5 C, (d) high-loading sulfur test at 0.3 C, and (e) rate capability test.

coated separator exhibits a lower polarization potential ($\Delta V =$ 0.20 V) as compared to that of the cell containing the rGO-N-CNTs-coated separator ($\Delta V = 0.35$ V) (Figure 5b). These observations predict higher specific discharge capacities for the cell featuring the a-VO$_x$@rGO-N-CNTs-coated separator relative to those for the cell comprising the rGO-N-CNTs-coated separator. To verify the CV results, initial charge–discharge potential profiles were obtained at 0.1 C (Figure 5b). The corresponding plateaus confirm that the electrochemical reactions are in appropriate agreement with the acquired peak positions in the CV curves. Cells with the a-VO$_x$@rGO-N-CNTs-coated separators demonstrated extended charge–discharge plateaus, indicating higher discharge capacities of these cells owing to their better redox reactions. Correspondingly, the Li-S cells consisting of a-VO$_x$@rGO-N-CNTs- and rGO-N-CNTs-coated separators delivered initial discharge capacities of 1084 and 798 mA h g^{-1}, respectively, at 0.1 C. Rapid redox reaction of the cell containing the a-VO$_x$@rGO-N-CNTs-coated separator as compared to that of the cell comprising the rGO-N-CNTs-coated separator can be ascribed to the synergistic effect of the highly conductive mesoporous framework comprising adequately entangled rGO and N-CNTs and the presence of multiple chemisorption sites in the forms of polar components (namely, a-VO$_x$ and metallic Co–Fe alloy). Moreover, heteroatom-doped CNTs serve as additional polarity sites, enhancing the overall LiPSs anchoring ability of the nanostructure.

Cycling performances of the Li-S cells utilizing different separators were also evaluated at 0.5 C, as shown in Figure 5c and Figure S7c. Cell with the a-VO$_x$@rGO-N-CNTs-coated separator exhibits an initial discharge capacity of 731 mA h g^{-1} (43.6% of the theoretical value) at 0.5 C, whereas the cell with the rGO-N-CNTs-coated separator demonstrates a lower initial discharge capacity of 711 mA h g^{-1}. At the end of the 400th cycle, the cells employing a-VO$_x$@rGO-N-CNTs- and rGO-N-CNTs-coated separators retain 63.7% (466 mA h g^{-1}) and 49.6% (353 mA h g^{-1}) of their initial capacities, respectively. Additionally, the average discharge capacity loss per cycle for the cell utilizing the a-VO$_x$@rGO-N-CNTs-coated separator is 0.09% compared to 0.13% for the cell comprising the rGO-N-CNTs-coated separator. To optimize the a-VO$_x$ content, a solution containing 3.0 g vanadyl acetylacetonate was impregnated into rGO-N-CNTs and then oxidized to synthesize excessive-a-VO$_x$@rGO-N-CNTs (denoted as Ex-a-VO$_x$@rGO-N-CNTs). As shown in Figure S7a,b, Ex-a-VO$_x$@rGO-N-CNTs exhibit a severely aggregated morphology. The cell with the Ex-a-VO$_x$@rGO-N-CNTs-coated separator showed an initial discharge capacity of 635 mA h g^{-1} at 0.5 C (Figure S7c). However, after 400 cycles, the discharge capacity of 323 mA h g^{-1} (average decay rate of 0.15% per cycle), indicating that excessive amounts of a-VO$_x$ can reduce long-term stability. This suggests that the excessive a-VO$_x$ leads to material agglomeration during cycling, and the reduced specific surface area does not effectively mitigate volume expansion. Consequently, this configuration is not suitable for long-term cycling.

The stable cycling performance of the cell featuring rGO-N-CNTs-coated separator is attributed to the presence of metallic Co–Fe alloy and higher specific surface areas of rGO-N-CNTs, slightly facilitating both chemical and physical adsorptions of intermediate polysulfides; however, to a lower extent. This reduces the active material utilization due to unfavorable redox reactions and leads to relatively inferior discharge capacity retention during long-term cycling. This is evidenced by the charge–discharge potential profiles acquired at various cycle intervals for the cells consisting of different coated separators, as depicted in Figure S8a,c. To thoroughly evaluate the capacity and performance enhancement effect of the modified separator, cycling tests were performed using a Li-S cell with a pristine separator that was not coated with any material (Figure S9). The Li-S cell using pristine separators exhibited poor capacity retention and overall cycling performance compared to those with modified separators. This deficiency is due to the lack of active sites required to adsorb LiPSs, leading to the loss of active material and subsequent capacity degradation. In contrast, the modified separators provide these active sites, resulting in improved performance and stability, as demonstrated in Figure 5c. The cell employing the a-VO_x@rGO-N-CNTs-coated separator actively anchored soluble LiPSs due to the presence of extra polar components, increasing the utilization of active materials and improving the discharge capacity. Furthermore, the a-VO_x@rGO-N-CNTs-coated separator demonstrates an average energy efficiency of 73.1%, indicating the high reversibility of redox reactions, whereas the energy efficiency for the cell with the rGO-N-CNTs-coated separator was 69.7%. In addition, as shown in Figure S8a,c, the voltage efficiency of the cell employing the a-VO_x@rGO-N-CNTs-coated separator was measured as 87.7%, reflecting reduced polarization during cycling, in contrast to 82.6% for the cell with the rGO-N-CNTs-coated separator. This highlights the enhanced electrochemical processes between Li_2S and elemental S promoted by a-VO_x during prolonged cycling. Cycling performance trends are similar even at a high current density of 1.0 C, as observed in Figure S10. After the activation steps, the initial discharge capacities of the cells utilizing the a-VO_x@rGO-N-CNTs- and rGO-N-CNTs-coated separators were measured as 567 and 585 $mA\,h\,g^{-1}$, respectively. However, after 800 cycles, the cell featuring the a-VO_x@rGO-N-CNTs-coated separator exhibits a lower capacity decay (0.09%, 160 $mA\,h\,g^{-1}$) as compared to that of the cell comprising the rGO-N-CNTs-coated separator (0.11%, 79 $mA\,h\,g^{-1}$), indicating superior active material utilization during cycling in the case of the cell with the a-VO_x@rGO-N-CNTs-coated separator. This is supported by the charge–discharge potential profiles, as shown in Figure S8b,d. Therefore, the improved cycling performances of the cell with the a-VO_x@rGO-N-CNTs-coated separator at both low and high C-rates again demonstrate the structural advantages of a-VO_x@rGO-N-CNTs. Furthermore, to verify the operational efficiencies of the functional interlayers, the cycling performances of the cells containing high sulfur loading electrodes (2.05 $mg\,cm^{-2}$) and low electrolyte/sulfur ratios (15 $\mu L\,mg^{-1}$) were also assessed at a C-rate of 0.3 C (Figure 5d). The relatively lower capacity of the a-VO_x@rGO-N-CNTs-coated separator up to 200 cycles can be attributed to the reduced porosity caused by the impregnation of a-VO_x, which increases the diffusion length for charged species under these challenging conditions. However, by the 500th cycle, the Li-S cells utilizing the a-VO_x@rGO-N-CNTs-coated separator exhibit a discharge capacity of 274 $mA\,h\,g^{-1}$, while the cell with the rGO-N-CNTs-coated separator shows a discharge capacity of 57 $mA\,h\,g^{-1}$. The corresponding average discharge capacity retentions of 45.7% and 8.0%, respectively. Similarly, the voltage and energy efficiency of the cell employing the a-VO_x@rGO-N-CNTs-coated separator were measured as 86.2% and 72.5%, respectively, demonstrating enhanced performance compared to 84.1% and 69.8% for the cell with the rGO-N-CNTs-coated separator. These results firmly validate the applicability of the a-VO_x@rGO-N-CNTs-coated separator paired with high sulfur content and ultra-low electrolyte volume for feasible applications.

Rate capability tests of the Li-S cells were also conducted at several C-rates ranging from 0.1 to 1.5 C (Figure 5e and Figure S7d). The cell using a-VO_x@rGO-N-CNTs-coated separator achieved discharge capacities of 952, 851, 779, 697, 613, 567, 528, and 473 $mA\,h\,g^{-1}$ at 0.1, 0.2, 0.3, 0.5, 0.7, 1.0, 1.2, and 1.5 C, respectively, at the fifth cycle of each C-rate. Comparatively, the cell employing rGO-N-CNTs-coated separator demonstrated discharge capacities of 917, 810, 737, 634, 481, 391, 325, and 227 $mA\,h\,g^{-1}$ at identical C-rates. Moreover, the average energy efficiency of the a-VO_x@rGO-N-CNTs-coated separator was consistently higher across all C-rates compared to that of the rGO-N-CNTs-coated separator, further demonstrating its improved operational efficiency. Detailed energy efficiency values for each C-rate are provided in Table S1, offering a comprehensive comparison of the separators' performance during the rate capability tests. Additionally, Ex-a-VO_x@rGO-N-CNTs-coated separator exhibited discharge capacities of 789, 665, 592, 515, 459, 422, 384, and 328 $mA\,h\,g^{-1}$ at the same C-rates. Notably, the two cells with a-VO_x@rGO-N-CNTs—and rGO-N-CNTs-coated separators exhibit similar discharge capacities at low current densities, primarily due to the high specific surface areas of rGO-N-CNTs that enable physical adsorption of LiPSs. However, the absence of a-VO_x as an additional polar material in rGO-N-CNTs causes inefficient trapping of the sulfur species thus resulting in LiPSs migration toward the anode. This leads to sustained active material loss and hence low discharge capacities, especially at high C-rates. In contrast, at high current densities (1.0 C and above), the cell with Ex-a-VO_x@rGO-N-CNTs-coated separator shows improved performance compared to the cell with rGO-N-CNTs-coated separator, demonstrating the beneficial role of the excess a-VO_x in capturing LiPSs and improving sulfur utilization. Despite this improvement at higher C-rates, Ex-a-VO_x@rGO-N-CNTs-coated separator does not perform as well overall as the different coated separator. Furthermore, when the C-rate recovers from 1.5 to 0.1 C, both a-VO_x@rGO-N-CNTs- and rGO-N-CNTs-coated separators demonstrate reversible discharge capacities of 855 $mA\,h\,g^{-1}$, whereas the cell with Ex-a-VO_x@rGO-N-CNTs-coated separator shows a lower capacity (681 $mA\,h\,g^{-1}$). This suggests that excess a-VO_x may hinder reversibility at low C-rates due to potential aggregation and supersaturation of the active sites, as well as increased pathways for charged species migration, leading to lower Coulombic efficiency and reduced specific capacity. The dramatic disparity in rate capability results of the two cells with a-VO_x@rGO-N-CNTs- and rGO-N-CNTs-coated separators is due to the presence of a-VO_x nanocrystals impregnated in the conductive matrix which effectively capture LiPSs species and mitigate the diffusion of these species toward the Li anode, thus improving sulfur utilization. Additionally, the highly entangled N-CNTs and rGO matrix promotes fast redox processes through the rapid migration of charged species. As shown in Table S2, the Li-S cell utilizing a-VO_x@rGO-N-CNTs-coated separator exhibited comparable or superior electrochemical properties compared to previously reported interlayer materials. Charge–discharge potential profiles of the cells with the a-VO_x@rGO-N-CNTs- (Figure S11a) and rGO-N-CNTs-coated separators (Figure S11b) acquired at various C-rates confirm the above results. Moreover, elemental S utilization bar charts were created for both cells at all C-rates, as shown in Figure S12. These bar charts clearly reveal that the cell employing the a-VO_x@rGO-N-CNTs-coated separator delivers higher capacity utilization, suggesting enhanced sulfur participation, supported by more kinetically efficient redox processes.

To examine the redox kinetics and Li-ion diffusion inside the Li-S cells with the a-VO_x@rGO-N-CNTs- and rGO-N-CNTs-coated separators, diffusion coefficient (D_{Li^+}) was determined via CV at various scan rates ranging from 0.1 to 0.5 $\mathrm{mV\,s^{-1}}$ (Figure 6a,c). CV curves obtained at various scan rates demonstrate typical Li-S redox peaks, indicating an electrochemical redox reaction between elemental S and Li_2S. Moreover, the CV curve of the cell with the a-VO_x@rGO-N-CNTs-coated separator exhibits higher current intensity redox peaks at all scan rates as compared to that of the cell with the rGO-N-CNTs-coated separator, thus implying strengthened redox kinetics along with rapid Li-ion diffusion. To further quantify the D_{Li^+} values, the Randles–Sevcik equation was applied in the following manner [22]:

$$I_p = 2.69 \times 10^5 n^{1.5} A D_{\mathrm{Li}^+}^{0.5} C_{\mathrm{Li}} \nu^{0.5}, \quad (1)$$

where I_p represents the redox current intensity, n is the number of electrons involved in the redox reaction ($n = 2$), A denotes the surface area of the electrode (cm^2), C_{Li} is the concentration of Li-ions ($\mathrm{mol\,L^{-1}}$), and ν represents the voltage scan rate ($\mathrm{V\,s^{-1}}$). Redox peak current (I_p) vs. voltage scan rate ($\nu^{0.5}$) curves acquired for the Li-S cell utilizing the a-VO_x@rGO-N-CNTs- and rGO-N-CNTs-coated separators are depicted in Figure 6b,d, respectively, and corresponding D_{Li^+} values for all the tested Li-S cells are provided in Table S3.

As observed, the cell paired with a-VO_x@rGO-N-CNTs-coated separator exhibits an ~1.8 times higher diffusion coefficient value ($5.13 \times 10^{-8}\ \mathrm{cm^2\,s^{-1}}$) compared to cell featuring rGO-N-CNTs-coated separator ($2.75 \times 10^{-8}\ \mathrm{cm^2\,s^{-1}}$). This indicates that the nanostructure comprising N-CNTs and rGO as a conductive matrix ensures rapid electron transfer during the electrochemical reaction, thereby improving the redox kinetics. Moreover, electrochemical impedance spectroscopy (EIS) profiles were used to further validate the reaction kinetics at the electrode–separator–electrolyte interface in the assembled Li-S cells before (Figure 6e) and after (Figure 6f) cycling. Additionally, the semicircles in the Nyquist plots were represented by the equivalent circuit model, which involved a combination of several parameters in both series and parallel configurations (Figure S13). Table S4 presents all EIS parameters for the Li-S cells with different coated separators before and after cycling. Impedance was evaluated for all the Li-S cells in fully charged states before cycling at an open-circuit voltage and at the end of the 400th cycle at 0.5 C. Li-S cells featuring different coated separators exhibit moderate solution resistance (R_s) values in a similar range (Figure 6e), implying similar interface environment between the electrode and electrolyte inside the cells. Furthermore, the cell utilizing the a-VO_x@rGO-N-CNTs-coated separator demonstrates a lower charge-transfer resistance (R_{ct}) of 23.0 Ω as compared to that of the cell with the rGO-N-CNTs-coated separator (42.7 Ω), followed by a slanted line related to the Li-ion diffusion. Additionally, after the 400th cycle (Figure 6f), the cell containing the a-VO_x@rGO-N-CNTs-coated separator exhibits a lower R_{ct} (21.0 Ω) than that of the cell with the rGO-N-CNTs-coated separator (36.6 Ω), suggesting efficient diffusion of charged species through the electrolyte. Notably, low R_{ct} of the cell with the a-VO_x@rGO-N-CNTs-coated separator led to a favorable redox process, thereby promoting efficient electrocatalytic conversion of LiPSs to elemental S and better electrochemical performance. Contrarily, the cell utilizing the rGO-N-CNTs-coated separator demonstrates weaker inhibition of polysulfide diffusion as compared to the case of the cell with the a-VO_x@rGO-N-CNTs-coated separator, clearly evidenced by the appearance of a distinct second semicircle in the Nyquist plot. These results prove that a-VO_x@rGO-N-CNTs as a functional interlayer not only improves the redox kinetics by facilitating charge transfer even after cycling, but also immobilizes LiPSs and ensures their catalytic conversion to elemental S, thus enhancing active material utilization.

To further assess the effect of the catalytic conversion in restricting the diffusion of LiPSs, symmetric cells and visual examination tests were also conducted. Symmetric cells were constructed using the a-VO_x@rGO-N-CNTs and rGO-N-CNTs electrodes as the counter and working electrodes and were filled with 20 μL of 0.33 M Li_2S_6 polysulfide solution. In Figure 7a, the initial CV curve obtained from a symmetric cell containing the a-VO_x@rGO-N-CNTs electrodes shows a redox peak with an elevated current intensity owing to the effective electrocatalytic conversions of LiPSs due to the existence of a-VO_x nanocrystals. Similar current intensities observed for the cell with the rGO-N-CNTs electrodes mainly arise from the effective physical trapping of LiPSs, facilitated by the extensive specific surface area of rGO-N-CNTs. Additionally, the metallic Co–Fe alloy in the host structure demonstrates electrocatalytic activity and offers a way of chemical immobilization. Moreover, overlapping CV curves of the cells with the a-VO_x@rGO-N-CNTs (Figure 7b) and rGO-N-CNTs electrodes (Figure 7c) confirm the above results, indicating consistent electrocatalytic properties of these cells during cycling. These

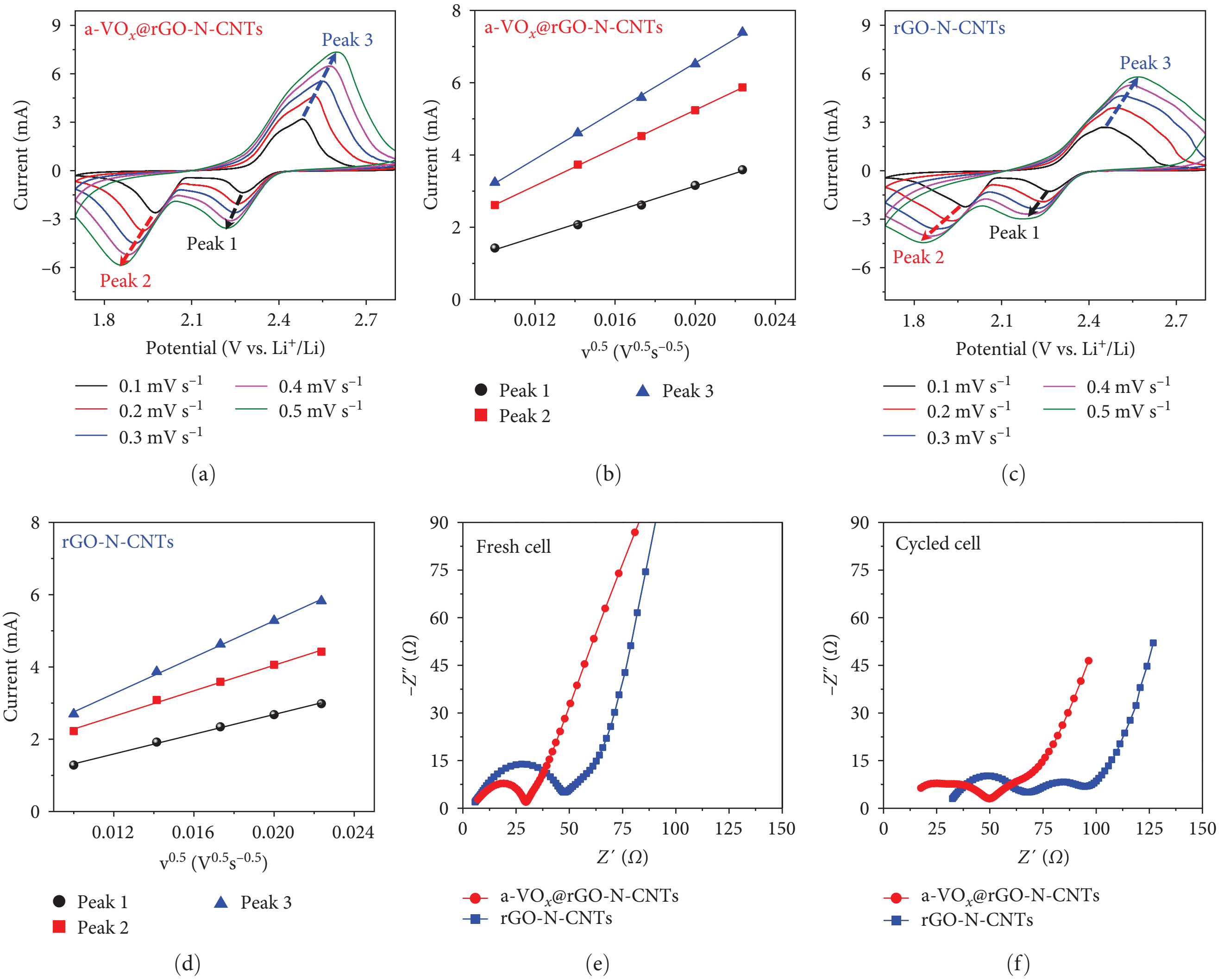

Figure 6: Lithium-ion diffusion coefficient (D_{Li^+}) and electrochemical impedance spectroscopy (EIS) spectra for the assembled Li-S cells with different coated separators: (a, c) cyclic voltammograms at various scan rates ranging from 0.1 to 0.5 mV s^{-1}, (b, d) peak current vs. square root of the voltage scan rate plots to calculate the D_{Li^+}; (e) EIS spectra of fresh cell, and (f) after 400th cycle at 0.5 C.

results were further validated by visual polysulfide capture tests, as shown in Figure 7d. Following the introductions of a-VO$_x$@rGO-N-CNTs and rGO-N-CNTs powders into the polysulfide solution, digital photographs were captured at various time intervals. The a-VO$_x$@rGO-N-CNTs powders exhibit a continuous color shift, transitioning from initial faded yellow ($T=0$) to nearly transparent after 1 h ($T=1$), contrary to the rGO-N-CNTs powders. This suggests efficient polysulfide capture in the cases of a-VO$_x$@rGO-N-CNTs powders, ascribed to the existence of impregnated a-VO$_x$ particles as well as metallic Co–Fe alloy in the interconnected N-CNTs and rGO structures, which act as polar entities to chemically anchor LiPSs. A schematic diagram showing the synthesized a-VO$_x$@rGO-N-CNTs powder as a functional interlayer is depicted in Figure 7e. The introduction of the coated separators not only overcomes the low electrical conductivity of the sulfur cathode but also ensures improved cell properties through the immobilization of LiPSs. The introduction of a functional interlayer, as indicated, ensures improved cell properties by trapping LiPSs toward the Li anode.

The improved trapping and faster electrocatalytic conversion of LiPSs by a-VO$_x$@rGO-N-CNTs-coated separator, compared to the pristine separator, were further demonstrated by FE-SEM analysis of the separator's morphology after disassembling the cell following 100 cycles at 0.5 C (Figure S14). Figure S14a,c presents FE-SEM images of a-VO$_x$@rGO-N-CNTs-coated separator and the pristine separator before cycling, respectively. The images show that a-VO$_x$@rGO-N-CNTs are uniformly coated over the entire separator (Figure S14a), while the pristine separator displays nanometer-sized open pores that allow Li-ion diffusion (Figure S14c). The FE-SEM image of a-VO$_x$@rGO-N-CNTs-coated separator after cycling, shown in Figure S14b, demonstrates that the spherical morphology is retained, indicating the robustness of the nanostructure. Additionally, the absence of polysulfide deposits suggests that the polysulfide species were effectively converted by a-VO$_x$

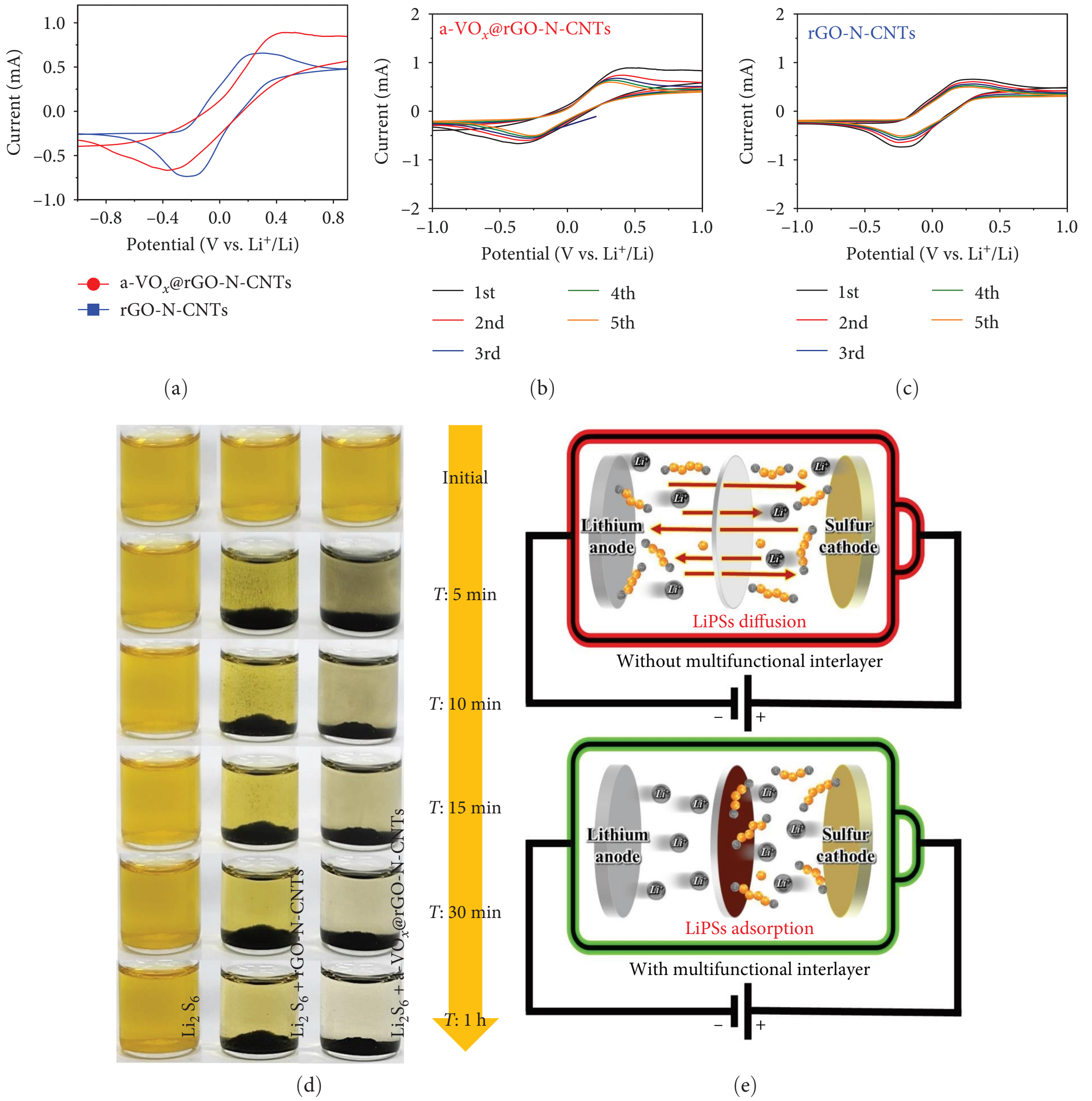

(a) (b) (c)

(d) (e)

Figure 7: Electrocatalytic activity and adsorption test of lithium polysulfides using a-VO$_x$@rGO-N-CNTs and rGO-N-CNTs powders: (a) initial CV curves of different symmetric cells at 0.1 mV s^{-1} in voltage ranging from –1.0 to 1.0 V, (b) five CV cycles for symmetric cell applying a-VO$_x$@rGO-N-CNTs, (c) five CV cycles for symmetric cell applying rGO-N-CNTs, (d) digital images of lithium polysulfide adsorption test over time, and (e) schematic illustrations of the lithium polysulfide trapping mechanism over the coated separators as functional interlayer.

nanoparticles and Co–Fe alloy. In contrast, the pristine separator (Figure S14d) shows significant polysulfide deposits due to the lack of material to trap LiPSs. This results in poor sulfur utilization and a significant degradation of electrochemical properties.

4. Conclusions

In this study, a-VO$_x$@rGO-N-CNTs were proposed as functional interlayers for LSBs for the first time. Hierarchical framework composed of rGO and N-CNTs with high specific surface areas was not only advantageous for the physical absorption of LiPSs but was also effective in suppressing volume changes in the active material. Additionally, the uniformly grown N-CNTs afforded highly conductive pathways, promoting charge mobility and rapid redox reactions. Finally, the introduction of a-VO$_x$ nanoparticles into rGO-N-CNTs maximized the synergistic effect of rGO and the N-CNT framework that efficiently regulated the diffusion of LiPSs and elevated active material utilization by facilitating the conversion of LiPSs to elemental S. Assembled Li-S cell utilizing the a-VO$_x$@rGO-N-CNT-coated separator demonstrates outstanding rate capability and stable cycling performance (an average discharge capacity loss of only 0.09% per cycle at 0.5 C after 400 cycles). Consequently, the design strategy proposed in this work provides valuable insights into the development of porous and conductive nanostructures for a wide range of energy storage applications including LSBs, while identifying the need for further advancements to achieve ultra-high sulfur loading mass ($>5\ \mathrm{mg\ cm^{-2}}$) and ultra-low E/S ratios ($<5\ \mu\mathrm{L\ mg^{-1}}$) for practical applications. This work establishes a foundation for future research dedicated to optimizing interlayer performance under these conditions, thereby facilitating progress toward the commercial implementation of LSB.

Data Availability Statement

The data used to support the findings of this study are included within the manuscript and the supporting information files.

Conflicts of Interest

The authors declare no conflicts of interest.

Author Contributions

Kun Woo Baek and Sang-Hyun Kim contributed equally to this work. Prof. Gi Dae Park and Jung Sang Cho were co-corresponding authors in this work.

Funding

This work was supported by the National Research Foundation of Korea (NRF) (grant no.: RS-2023-00217581) and the Commercialization Promotion Agency for R&D Outcomes (COMPA) funded by the Ministry of Science and ICT (grant no.: RS-2023-00304768). Following are results of a study on the "Leaders in Industry-university Cooperation 3.0" project, supported by the Ministry of Education and the National Research Foundation of Korea. This research was supported by Chungcheongbuk-do Province and Convergence and Open Sharing System (COSS) Development Project (2023).

Supporting Information

Additional supporting information can be found online in the Supporting Information section. (*Supporting Information*) The supporting information file contains detailed experimental results for this paper. It includes the following information. Figure S1. Morphologies and XRD pattern of crumpled rGO microspheres obtained after spray pyrolysis: (a, b) FE-SEM images and (c) XRD pattern. Figure S2. XRD patterns of a-VO_x@rGO-N-CNTs and rGO-N-CNTs microspheres. Figure S3. XRD pattern of rGO-N-CNTs microspheres after TG analysis. Figure S4. (a, c) N_2 adsorption–desorption isotherms and (b, d) BJH pore size distribution curve for a-VO_x@rGO-N-CNTs and rGO-N-CNTs microspheres. Figure S5. Digital photographs: (a) the coated separator and (b) flexibility and integrity test of a-VO_x@rGO-N-CNTs-coated separator and cross-sectional FE-SEM images: (c) pristine separator and (d) a-VO_x@rGO-N-CNTs-coated separator. Figure S6. First five CV curves of (a) a-VO_x@rGO-N-CNTs and (b) rGO-N-CNTs at a scan rate of $0.05\ \mathrm{mV\ s^{-1}}$. Figure S7. FE-SEM image of Ex-a-VO_x@rGO-N-CNTs with (a) low-, (b) high-magnification. Electrochemical properties of Ex-a-VO_x@rGO-N-CNTs for Li-S cell: (c) cycle performance of the assembled cell at 0.5 C and (d) rate capability test. Figure S8. Respective charge–discharge potential profiles of the Li-S cells with different interlayer at 0.5 and 1.0 C: (a, b) a-VO_x@rGO-N-CNTs and (c, d) rGO-N-CNTs. Figure S9. Cycling performance of the assembled Li-S cell with pristine separator at 0.5 C. Figure S10. Prolonged cycle performance of the Li-S cell employing a-VO_x@rGO-N-CNTs and rGO-N-CNTs at high current density (1.0 C). Table S1. Average Coulombic efficiencies of Li-S cells utilizing different separators at various C-rates during rate capability tests. Table S2. Comparison of the electrochemical properties of Li-S cell utilizing a-VO_x@rGO-N-CNTs-coated separator with the previously reported interlayer materials. Figure S11. Respective charge–discharge potential profiles at various current density for (a) a-VO_x@rGO-N-CNTs and (b) rGO-N-CNTs. Figure S12. Capacity utilization bar charts of the Li-S cells with a-VO_x@rGO-N-CNTs and rGO-N-CNTs-coated separators at different current density. Table S3. Lithium-ion diffusion coefficient ($D_{\mathrm{Li^+}}$) for the Li-S cells utilizing different coated separators. Figure S13. Equivalent circuit fitting model for Li-S cells: (a) before cycling and (b) after cycling. Table S4. EIS parameters for the Li-S cells employing different coated separators before cycle, and after 400th cycle at 0.5C. Figure S14. The FE-SEM images of a-VO_x@rGO-N-CNTs-coated separator and pristine separator after cycling at 0.5 C rate: (a, c) before cycle and (b, d) after 100th cycle.

References

[1] S. Ghosh, W. D. Yong, E. M. Jin, S. R. Polaki, S. M. Jeong, and H. Jun, "Mesoporous Carbon Nanofiber Engineered for Improved Supercapacitor Performance," *Korean Journal of Chemical Engineering* 36, no. 2 (2019): 312–320.

[2] J. Hassoun, K.-S. Lee, Y.-K. Sun, and B. Scrosati, "An Advanced Lithium Ion Battery Based on High Performance Electrode Materials," *Journal of the American Chemical Society* 133, no. 9 (2011): 3139–3143.

[3] T. Kim, W. Song, D.-Y. Son, L. K. Ono, and Y. Qi, "Lithium-Ion Batteries: Outlook on Present, Future, and Hybridized Technologies," *Journal of Materials Chemistry A* 7, no. 7 (2019): 2942–2964.

[4] Y. Liang, C. Z. Zhao, H. Yuan, et al., "A Review of Rechargeable Batteries for Portable Electronic Devices," *InfoMat* 1, no. 1 (2019): 6–32.

[5] R. Saroha, J. H. Oh, Y. H. Seon, et al., "Freestanding Interlayers for Li-S Batteries: Design and Synthesis of Hierarchically Porous N-Doped C Nanofibers Comprising Vanadium Nitride Quantum Dots and MOF-Derived Hollow N-Doped C Nanocages," *Journal of Materials Chemistry A* 9, no. 19 (2021): 11651–11664.

[6] B. Scrosati, "Power Sources for Portable Electronics and Hybrid Cars: Lithium Batteries and Fuel Cells," *The Chemical Record* 5, no. 5 (2005): 286–297.

[7] A. M. Suzanowicz, C. W. Mei, and B. K. Mandal, "Approaches to Combat the Polysulfide Shuttle Phenomenon in Li-S Battery Technology," *Batteries* 8, no. 5 (2022): 45.

[8] L. Zhang, W. Wang, S. Lu, and Y. Xiang, "Carbon Anode Materials: A Detailed Comparison Between Na-Ion and K-Ion Batteries," *Advanced Energy Materials* 11, no. 11 (2021): 2003640.

[9] L. Gao, M. Cao, Y. Q. Fu, Z. Zhong, Y. Shen, and M. Wang, "Hierarchical TiO_2 Spheres Assisted With Graphene for a High

Performance Lithium-Sulfur Battery," *Journal of Materials Chemistry A* 4 (2016): 16454–16461.

[10] Z. A. Ghazi, X. He, A. M. Khattak, et al., "MoS_2/Celgard Separator as Efficient Polysulfide Barrier for Long-Life Lithium-Sulfur Batteries," *Advanced Materials* 29, no. 21 (2017): 1606817.

[11] R. Saroha, J. H. Oh, J. S. Lee, et al., "Hierarchically Porous Nanofibers Comprising Multiple Core-Shell Co_3O_4@graphitic Carbon Nanoparticles Grafted Within N-Doped CNTs as Functional Interlayers for Excellent Li-S Batteries," *Chemical Engineering Journal* 426 (2021): 130805.

[12] J. Song, Z. Yu, T. Xu, et al., "Flexible Freestanding Sandwich-Structured Sulfur Cathode With Superior Performance for Lithium-Sulfur Batteries," *Journal of Materials Chemistry A* 2, no. 23 (2014): 8623–8627.

[13] C. Deng, Z. Wang, L. Feng, S. Wang, and J. Yu, "Electrocatalysis of Sulfur and Polysulfides in Li-S Batteries," *Journal of Materials Chemistry A* 8, no. 38 (2020): 19704–19728.

[14] R. Fang, S. Zhao, Z. Sun, D-W. Wang, H-M. Cheng, and F. Li, "More Reliable Lithium-Sulfur Batteries: Status, Solutions and Prospects," *Advanced Materials* 29, no. 48 (2017): 1606823.

[15] C. Li, Z. Xi, D. Guo, X. Chen, and L. Yin, "Chemical Immobilization Effect on Lithium Polysulfides for Lithium-Sulfur Batteries," *Small* 14, no. 4 (2018): 1701986.

[16] S. Tu, X. Zhao, M. Cheng, P. Sun, Y. He, and Y. Xu, "Uniform Mesoporous MnO_2 Nanospheres as a Surface Chemical Adsorption and Physical Confinement Polysulfide Mediator for Lithium-Sulfur Batteries," *ACS Applied Materials & Interfaces* 11, no. 11 (2019): 10624–10630.

[17] F. Li, Q. Liu, J. Hu, Y. Feng, P. He, and J. Ma, "Recent Advances in Cathode Materials for Rechargeable Lithium-Sulfur Batteries," *Nanoscale* 11, no. 33 (2019): 15418–15439.

[18] S. Li, W. Zhang, J. Zheng, M. Lv, H. Song, and L. Du, "Inhibition of Polysulfide Shuttles in Li-S Batteries: Modified Separators and Solid-State Electrolytes," *Advanced Energy Materials* 11, no. 2 (2021): 2000779.

[19] H. Raza, S. Bai, J. Cheng, et al., "Li-S Batteries: Challenges, Achievements and Opportunities," *Electrochemical Energy Reviews* 6 (2023): 29.

[20] S. Yang, R. Xiao, T. Hu, et al., "Ni_2P Electrocatalysts Decorated Hollow Carbon Spheres as Bi-Functional Mediator Against Shuttle Effect and Li Dendrite for Li-S Batteries," *Nano Energy* 90 (2021): 106584.

[21] H. Ahn, Y. Kim, J. Bae, Y. K. Kim, and W. B. Kim, "A Multifunctional SnO_2-Nanowires/Carbon Composite Interlayer for High-Performance Lithium-Sulfur Batteries," *Chemical Engineering Journal* 401 (2020): 26042.

[22] J. M. Choi, R. Saroha, J. S. Kim, M. R. Jang, and J. S. Cho, "Porous Nanofibers Comprising VN Nanodots and Densified N-Doped CNTs as Redox-Active Interlayers for Li-S Batteries," *Journal of Power Sources* 559 (2023): 232632.

[23] M. S. Garapati and R. Sundara, "Enhancing Polysulfide Confinement and Redox Kinetics by Electrocatalytic Interlayer for Highly Stable Lithium-Sulfur Batteries," *Electrochimica Acta* 362 (2020): 137035.

[24] P. Guo, K. Sun, X. Shang, et al., "Nb_2O_5/RGO Nanocomposite Modified Separators With Robust Polysulfide Traps and Catalytic Centers for Boosting Performance of Lithium-Sulfur Batteries," *Small* 15, no. 40 (2019): 1902363.

[25] G. Liang, J. Wu, X. Qin, et al., "Ultrafine TiO_2 Decorated Carbon Nanofibers as Multifunctional Interlayer for High-Performance Lithium-Sulfur Battery," *ACS Applied Materials & Interfaces* 8, no. 35 (2016): 23105–23113.

[26] A. A. Razzaq, Y. Yao, R. Shah, et al., "High-Performance Lithium Sulfur Batteries Enabled by a Synergy Between Sulfur and Carbon Nanotubes," *Energy Storage Materials* 16 (2019): 194–202.

[27] W. Kang, L. Fan, N. Deng, et al., "Sulfur-Embedded Porous Carbon Nanofiber Composites for High Stability Lithium-Sulfur Batteries," *Chemical Engineering Journal* 333 (2018): 185–190.

[28] M.-Q. Zhao, Q. Zhang, J.-Q. Huang, et al., "Unstacked Double-Layer Templated Graphene for High-Rate Lithium-Sulphur Batteries," *Nature Communications* 5 (2014): 3410.

[29] X.-X. Peng, Y.-Q. Lu, L.-L. Zhou, et al., "Graphitized Porous Carbon Materials With High Sulfur Loading for Lithium-Sulfur Batteries," *Nano Energy* 32 (2017): 503–510.

[30] S. Chen, X. Huang, H. Liu, et al., "3D Hyperbranched Hollow Carbon Nanorod Architectures for High-Performance Lithium-Sulfur Batteries," *Advanced Energy Materials* 4, no. 8 (2014): 1301761.

[31] H. Jia, J. Fan, P. Su, T. Guo, and M. C. Liu, "Cobalt Nitride Nanoparticles Encapsulated in N-Doped Carbon Nanotubes Modified Separator of Li-S Battery Achieving the Synergistic Effect of Restriction-Adsorption-Catalysis of Polysulfides," *Small* 20, no. 26 (2024): 2311343.

[32] X. Jiang, S. Zhang, B. Zou, et al., "Electrospun CoSe@NC Nanofiber Membrane as an Effective Polysulfides Adsorption-Catalysis Interlayer for Li-S Batteries," *Chemical Engineering Journal* 430 (2022): 131911.

[33] Z. Shi, Z. Sun, J. Cai, et al., "Boosting Dual-Directional Polysulfide Electrocatalysis via Bimetallic Alloying for Printable Li-S Batteries," *Advanced Functional Materials* 31, no. 4 (2021): 2006798.

[34] R. Saroha, H. H. Choi, and J. S. Cho, "Boosting Redox Kinetics Using Rationally Engineered Cathodic Interlayers Comprising Porous rGO-CNT Framework Microspheres With $NiSe_2$-Core@ N-Doped Graphitic Carbon Shell Nanocrystals for Stable Li-S Batteries," *Chemical Engineering Journal* 473 (2023): 145391.

[35] S. Jiang, M. Chen, X. Wang, et al., "A Tin Disulfide Nanosheet Wrapped With Interconnected Carbon Nanotube Networks for Application of Lithium Sulfur Batteries," *Electrochimca Acta* 313 (2019): 151–160.

[36] R. Saroha, H. S. Ka, and J. S. Cho, "A Novel Three-Dimensional Ordered Mesoporous Microspheres Comprising N-Doped Graphitic Carbon-Coated Fe_xP Nanoparticles as Multifunctional Interlayers to Suppress Polysulfide Crossover in Li-S Batteries," *Applied Surface Science* 612 (2023): 155892.

[37] J. Wang and W. Q. Han, "A Review of Heteroatom Doped Materials for Advanced Lithium-Sulfur Batteries," *Advanced Functional Materials* 32, no. 2 (2022): 2107166.

[38] J. Qin, R. Wang, P. Xiao, and D. Wang, "Engineering Cooperative Catalysis in Li-S Batteries," *Advanced Energy Materials* 13, no. 26 (2023): 2300611.

[39] Z. Shi, Y. Yang, Y. Huang, et al., "Organic Alkali Metal Salt Derived Three-Dimensional N-Doped Porous Carbon/Carbon Nanotubes Composites With Superior Li-S Battery Performance," *ACS Sustainable Chemistry & Engineering* 7, no. 4 (2019): 3995–4003.

[40] Y. Ning, B. Wang, F. Jin, et al., "A Rational VO_2 Nanotube/Graphene Binary Sulfur Host for Superior Lithium-Sulfur Batteries," *Journal of Alloys and Compounds* 838 (2020): 155504.

[41] H. Wu, M. Xu, P. Da, W. Li, D. Jia, and G. Zheng, "WO_3–reduced Graphene Oxide Composites With Enhanced Charge Transfer for

Photoelectrochemical Conversion," *Physical Chemistry Chemical Physics* 15, no. 38 (2013): 16138–16142.

[42] G. Zhou, L. Li, C. Ma, et al., "A Graphene Foam Electrode With High Sulfur Loading for Flexible and High Energy Li-S Batteries," *Nano Energy* 11 (2015): 356–365.

[43] X. Li, Z. Pan, Z. Li, et al., "Coral-Like Reduced Graphene Oxide/Tungsten Sulfide Hybrid as a Cathode Host of High Performance Lithium-Sulfur Battery," *Journal of Power Sources* 420 (2019): 22–28.

[44] L. Luo, S.-H. Chung, and A. Manthiram, "Rational Design of a Dual-Function Hybrid Cathode Substrate for Lithium-Sulfur Batteries," *Advanced Energy Materials* 8, no. 24 (2018): 1801014.

[45] B. Yuan, C. Bao, X. Qian, et al., "Design of Artificial Nacre-Like Hybrid Films as Shielding to Mitigate Electromagnetic Pollution," *Carbon* 75 (2014): 178–189.

[46] B. Yuan, Y. Shi, X. Mu, et al., "A Facile Method to Prepare Reduced Graphene Oxide With a Large Pore Volume," *Materials Letters* 162 (2016): 154–156.

[47] L. Wang, Z.-Y. Wang, J.-F. Wu, G.-R. Li, S. Liu, and X.-P. Gao, "To Effectively Drive the Conversion of Sulfur With Electroactive Niobium Tungsten Oxide Microspheres for Lithium−Sulfur Battery," *Nano Energy* 77 (2020): 105173.

[48] Z. Wu, G. Zhou, L. Yin, W. Ren, and F. Li, "Graphene/Metal Oxide Composite Electrode Materials for Energy Storage," *Nano Energy* 1 (2012): 107–131.

[49] I. Shakir, "High Energy Density Based Flexible Electrochemical Supercapacitors From Layer-by-Layer Assembled Multiwall Carbon Nanotubes and Graphene," *Electrochimica Acta* 129 (2014): 396–400.

[50] F. Cheng, Y. Xu, J. Zhang, et al., "A Novel Flexible Carbon Fiber With Carbon Nanotubes Growing in-Situ via Chemical Vapor Deposition to Impregnate Paraffin for Thermal Energy Application," *Journal of Energy Storage* 68 (2023): 107718.

[51] J. Cui, S. Yao, J.-Q. Huang, et al., "Sb-Doped SnO_2/Graphene-CNT Aerogels for High Performance Li-Ion and Na-Ion Battery Anodes," *Energy Storage Materials* 9 (2017): 85–95.

[52] T. T. Tung, M. Moussa, K. M. Tripathi, et al., "Coupling Graphene Microribbons With Carbon Nanofibers: New Carbon Hybrids for High-Performing Lithium and Potassium-Ion Batteries," *Sustainable Materials and Technologies* 32 (2022): e00393.

[53] G. Ahmed, Z. H. Awan, F. A. Butt, et al., "The Study of Different Redox Mediators for Competent Li-Air Batteries," *Journal of Power Sources* 538 (2022): 231379.

[54] M. S. Jo, S. Ghosh, S. M. Jeong, Y. C. Kang, and J. S. Cho, "Coral-Like Yolk-Shell-Structured Nickel Oxide/Carbon Composite Microspheres for High-Performance Li-Ion Storage Anodes," *Nano-Micro Letters* 11 (2019): 3.

[55] S. Shi, Y. Yu, X. Feng, R. Qi, and Y. Zhao, "Two-Dimensional VO_2 Nanosheets With a Controllable Crystalline-Preferred Orientation for High-Performance Zinc-Ion Batteries," *Batteries* 9, no. 2 (2023): 95.

[56] J. H. Choi, J.-S. Park, and Y. C. Kang, "Macroporous Vanadium Dioxide-Reduced Graphene Oxide Microspheres: Cathode Material With Enhanced Electrochemical Kinetics for Aqueous Zinc-Ion Batteries," *Applied Surface Science* 599 (2022): 153890.

[57] J. Wang, X. Zhang, Y. Zhang, et al., "Lightweight, Interconnected VO_2 Nanoflowers Hydrothermally Grown on 3D Graphene Networks for Wide-Voltage-Window Supercapacitors," *RSC Advances* 7, no. 56 (2017): 35558–35564.

[58] Y. Dong, X. Niu, W. Song, et al., "Facile Synthesis of Vanadium Oxide/Reduced Graphene Oxide Composite Catalysts for Enhanced Hydroxylation of Benzene to Phenol," *Catalysts* 6, no. 5 (2016): 74.

[59] S.-H. Kim, T. H. Kim, H. K. Park, Y. C. Kang, J. S. Cho, and G. D. Park, "Aerosol-Assisted Synthesis of 3D Hybridized Reduced Graphene Oxide-Carbon Nanotube Composite Microsphere With Cobalt-Iron Selenide Nanocrystal as Anode Materials for Potassium-Ion Batteries," *Journal of Energy Storage* 83 (2024): 110683.

[60] S. Guo, S. Zhao, X. Wu, et al., "A Co_3O_4-CDots-C_3N_4 Three Component Electrocatalyst Design Concept for Efficient and Tunable CO_2 Reduction to Syngas," *Nature Communications* 8 (2017): 1828.

[61] M. Ren, J. Zhang, and J. M. Tour, "Laser-Induced Graphene Synthesis of Co_3O_4 in Graphene for Oxygen Electrocatalysis and Metal-Air Batteries," *Carbon* 139 (2018): 880–887.

[62] H. Tan, X. Liu, M. Wang, H. Huang, and P. Huang, "Co_3O_4 Supported on Graphene-Like Carbon by One-Step Calcination of Cobalt Phthalocyanine for Efficient Oxygen Reduction Reaction under Alkaline Medium," *Nanomaterials* 13, no. 7 (2023): 1241.

[63] H. Lee, W.-J. Lee, Y.-K. Park, S. J. Ki, B.-J. Kim, and S.-C. Jung, "Liquid Phase Plasma Synthesis of Iron Oxide Nanoparticles on Nitrogen-Doped Activated Carbon Resulting in Nanocomposite for Supercapacitor Applications," *Nanomaterials* 8, no. 4 (2018): 190.

[64] M. S. Jo, J. S. Lee, S. Y. Jeong, et al., "Golden Bristlegrass-Like Hierarchical Graphene Nanofibers Entangled With N-Doped CNTs Containing $CoSe_2$ Nanocrystals at Each Node as Anodes for High-Rate Sodium-Ion Batteries," *Small* 16, no. 38 (2020): e2003391.

[65] J. S. Lee, R. Saroha, J. H. Oh, et al., "Camphene-Derived Hollow and Porous Nanofibers Decorated With Hollow NiO Nanospheres and Graphitic Carbon as Anodes for Efficient Lithium-Ion Storate," *Journal of Industrial and Engineering Chemistry* 114 (2022): 276–287.

[66] Y. Zhang, X. Yin, H. Jiang, et al., "Cobalt Nanoparticles Embedded in Nitrogen-Doped Carbon Nanotubes for Efficient Catalysis of Oxygen Reduction Reaction," *Journal of the Iranian Chemical Society* 16 (2019): 2575–2585.

[67] R. Saroha, Y. H. Seon, B. Jin, et al., "Self-Supported Hierarchically Porous 3D Carbon Nanofiber Network Comprising Ni/Co/$NiCo_2O_4$ Nanocrystals and Hollow N-Doped C Nanocages as Sulfur Host for Highly Reversible Li-S Batteries," *Chemical Engineering Journal* 446 (2022): 137141.

[68] P. Wu, L. Tan, X.-D. Wang, et al., "Porous 3D Nitrogen-Doped rGO/Co-Ni-S Composite Modified Separator for High-Capacity and Stable Lithium-Sulfur Batteries," *Materials Research Bulletin* 145 (2022): 111550.

[69] D. Liu, C. Wu, M. Yan, and J. Wang, "Correlating the Microstructure, Growth Mechanism and Magnetic Properties of FeSiAl Soft Magnetic Composites Fabricated via HNO_3 Oxidation," *Acta Materialia* 146 (2018): 294–303.